Title
Histone Deacetylase 8: Characterization of Physiological Divalent Metal Catalysis

Journal
The Journal of Physical Chemistry B, 120(26)

ISSN
1520-6106

Authors
Nechay, Michael R
Gallup, Nathan M
Morgenstern, Amanda
et al.

Publication Date
2016-07-07

DOI
10.1021/acs.jpcb.6b00997

Peer reviewed

THE JOURNAL OF PHYSICAL CHEMISTRY B

Article

pubs.acs.org/JPCB

Histone Deacetylase 8: Characterization of Physiological Divalent Metal Catalysis

Michael R. Nechay,[†] Nathan M. Gallup,[†] Amanda Morgenstern,[‡] Quentin A. Smith,[†] Mark E. Eberhart,[‡] and Anastassia N. Alexandrova*[,†,§]

[†]Department of Chemistry and Biochemistry, University of California, Los Angeles, Los Angeles, California 90095, United States

[‡]Molecular Theory Group, Colorado School of Mines, Golden, Colorado 80401, United States

[§]California NanoSystems Institute, Los Angeles, California 90095, United States

Supporting Information

ABSTRACT: Histone deacetylases (HDACs) are responsible for the removal of acetyl groups from histones, resulting in gene silencing. Overexpression of HDACs is associated with cancer, and their inhibitors are of particular interest as chemotherapeutics. However, HDACs remain a target of mechanistic debate. HDAC class 8 is the most studied HDAC, and of particular importance due to its human oncological relevance. HDAC8 has traditionally been considered to be a Zn-dependent enzyme. However, recent experimental assays have challenged this assumption and shown that HDAC8 is catalytically active with a variety of different metals, and that it may be a Fe-dependent enzyme *in vivo*. We studied two opposing mechanisms utilizing a series of divalent metal ions in physiological abundance (Zn^{2+}, Fe^{2+}, Co^{2+}, Mn^{2+}, Ni^{2+}, and Mg^{2+}). Extensive sampling of the entire protein with different bound metals was done with the mixed quantum-classical QM/DMD method. Density functional theory (DFT) on an unusually large cluster model was used to describe the active site and reaction mechanism. We have found that the reaction profile of HDAC8 is similar among all metals tested, and follows one of the previously published mechanisms, but the rate-determining step is different from the one previously claimed. We further provide a scheme for estimating the metal binding affinities to the protein. We use the quantum theory of atoms in molecules (QTAIM) to understand the different binding affinities for each metal in HDAC8 as well as the ability of each metal to bind and properly orient the substrate for deacetylation. The combination of this data with the catalytic rate constants is required to reproduce the experimentally observed trend in metal-depending performance. We predict Co^{2+} and Zn^{2+} to be the most active metals in HDAC8, followed by Fe^{2+}, and Mn^{2+} and Mg^{2+} to be the least active.

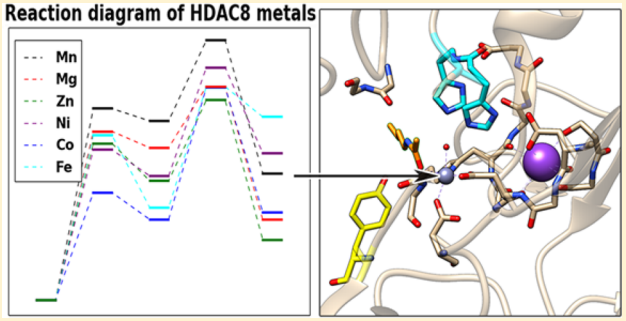

INTRODUCTION

The acetylation of lysine residues is an important reversible post-translational modification that modulates protein function, affecting a variety of cellular processes.[1−5] Proteomic surveys[6−8] have identified acetyl-lysine residues in diverse groups of proteins, including transcription factors,[9,10] cell signaling proteins,[11] metabolic enzymes (most prominently acetyl-CoA synthase[12−14]), structural proteins in the cytoskeleton,[15,16] and HIV viral proteins.[17,18]

One of the first discovered examples of lysine acetylation was that occurring in histones,[19,20] the predominant protein components of chromatin. Acetylation of histones has been linked to gene regulation: the addition of an acetyl moiety to histone lysine residues gives rise to an open chromatin structure that facilitates DNA transcription, while the removal of acetyl from histone acetyl-lysine residues is associated with a closed chromatin structure, transcriptional repression, and gene silencing.[21] The enzymes responsible for the addition and removal of acetyl groups are known as histone acetyltransferases (HATs) and histone deacetylases (HDACs)[22−26] for historical reasons, although it is now recognized that some of them may act on nonhistone proteins as well.[1,3,4]

Because overexpression of HDACs is associated with pathological states, including cancer, HDACs are of interest as drug targets.[24,27−30] Inhibition of HDACs results in histone hyperacetylation and transcriptional activation of genes that are linked to growth arrest and apoptosis in tumor cells.[31] Suberoylanilide hydroxamic acid (SAHA), a HDAC inhibitor that coordinates directly to the catalytic metal ion of zinc-dependent HDACs, was approved by the FDA as an anticancer drug in 2006.[24]

HDACs are classified into four subtypes based on phylogenetic similarity.[32] Classes I, II, and IV are zinc-

Special Issue: William M. Gelbart Festschrift

Received: January 29, 2016
Revised: March 19, 2016
Published: March 21, 2016

DOI: 10.1021/acs.jpcb.6b00997
J. Phys. Chem. B 2016, 120, 5884−5895

dependent hydrolases, while members of class III are NAD^+-dependent and do not contain a catalytic metal ion. Of the zinc-dependent HDACs, histone deacetylase 8 (HDAC8) is the best-characterized by experiment.[33−39] X-ray crystal structures of several HDAC8 enzyme−inhibitor and mutant−substrate complexes have been obtained.[33−36]

The crystal structure of the HDAC8 Y306F mutant, in complex with an acetylated lysine substrate (PDB accession code 2V5W),[35] illustrates the key residues involved in deacetylation (Figure 1). The active site of HDAC8 contains

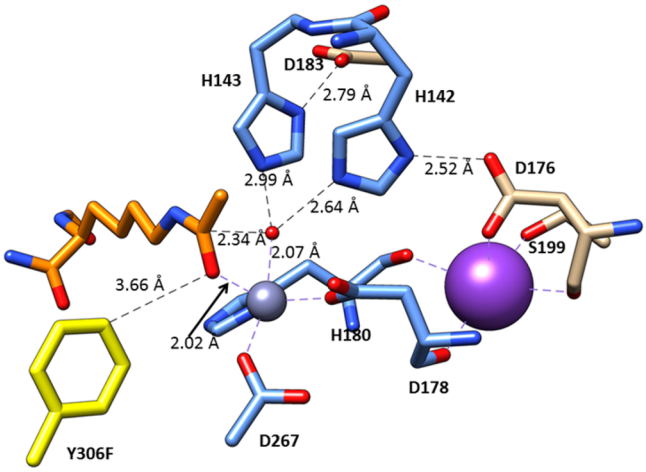

Figure 1. Active site of HDAC8 extracted from the crystal structure (PDB code 2V5W), highlighting the most critical residues relevant to catalysis within the active site. In this work, F306 was reverted to tyrosine to facilitate catalysis (yellow, Y306F). Blue residues participate directly in catalysis or coordination of the divalent metal ion, the orange residue is the crystal structure substrate, and represented in purple is a nearby K ion surrounded by a small net of residues holding it in place.

a metal-binding center that is coordinated to one histidine (H180) and two aspartate (D178 and D267) residues. A water molecule, which is present in the crystal structure, coordinates with the zinc and is associated with two additional histidine residues, H142 and H143. These histidines form dyads with the aspartates D176 and D183, respectively. Given that the mutation of residue 306 from tyrosine to phenylalanine is sufficient to render the enzyme inactive, this residue must also play a role in the deacetylation process. In the crystal structure, the acetyl-lysine substrate appears coordinated to the zinc, with a carbonyl oxygen (R(Zn−O) = 2.02 Å).

Previously suggested reaction mechanisms for the deacetylation process include a general acid−base catalytic pair mechanism[25,40] and a proton shuttle catalytic mechanism.[41] These mechanisms were hypothesized on the basis of previous studies of histone deacetylase-like protein (HDLP),[22,42] a homologue of HDAC found in hyperthermophilic bacteria. In the general acid−base mechanism (Figure 2, mechanism a), a singly protonated H142 acts as a base, abstracting a proton from the water molecule, while a doubly protonated H143 acts as an acid, donating a proton to the substrate nitrogen.[22,23] The acetyl group leaves in conjunction with nitrogen protonation. This mechanism relies on an unusual (at neutral pH) protonation state for H143 that is not supported by theoretical calculations.[41,43] In the proton shuttle mechanism (Figure 2, mechanism b), H142 and H143 are initially singly protonated. H143 alternates between acting as a base and acting as an acid, first abstracting a proton from water and subsequently transferring it to the substrate nitrogen.[41]

While HDAC8 is of interest as a drug target inhibitor for pathological treatments, there has been a small amount of theoretical analysis surrounding the mechanism by which HDAC8 catalysis functions. Parallels have been drawn between the active site of serine proteases and HDAC8.[22] The nature of the active site has led to a variety of mechanistic speculations and hypotheses that have been examined theoretically.[41,42] Most of these prior investigations utilized mixed quantum mechanical/molecular mechanical (QM/MM) methods to elucidate HDAC8's mode of catalysis. Expensive *ab initio* Born−Oppenheimer molecular dynamics has been used,[45] but the computational expense was so high that the active site had to be significantly truncated, and the effects of the nearby potassium ion and potassium-binding pocket were included only as an electrostatic correction post-sampling. The role K^+ plays in HDAC8 catalysis is a contentious matter. Theoretical investigations have concluded that this K^+ has a stabilizing electrostatic effect;[41] however, experimental studies have claimed potentially inhibitory effects.[38] These mechanistic studies have also sought to examine the impact of the His−Asp dyads that coordinate directly to an active site water likely involved in catalysis. Generally, it has been found that these dyad contacts are necessary to facilitate adequate basicity of the participating His residues. Computational studies thus far have centered exclusively on the hypothesis that HDAC8 functions as a native Zn^{2+} enzyme. However, Gantt et al.[37] demonstrated that HDAC8 functions with a variety of physiological divalent metals, and suggested that HDAC8 may be an Fe^{2+} dependent enzyme, contrary to all published theoretical models, currently.

In this study, we examine how HDAC8 may function when utilizing several different divalent metal ions, Co^{2+}, Fe^{2+}, Zn^{2+}, Ni^{2+}, Mg^{2+}, and Mn^{2+}. Analyzing a variety of metals is important because it has previously been shown that different metals are capable of facilitating alternative enzymatic functions.[44] Our model relies on a mixed quantum-classical description, and utilizes the largest published QM active site, which reveals significant differences in the catalytic profile from previously published theoretical results. We also examine the role that the nearby K^+ and its binding pocket and the active site His−Asp dyads may play in catalysis. We will also discuss the capabilities of each metal to bind to HDAC8, and how that may influence apparent catalysis *in vivo*.

■ COMPUTATIONAL METHODS

The initial structure of HDAC8 was obtained from the crystal structure of the Y306F mutant (PDB accession code 2V5W).[35] Residue 306 was transformed from phenylalanine to tyrosine using UCSF Chimera. The protonation states of all residues were chosen in accord with their pK_a values at neutral pH, including singly protonated His180 on the δ site, and singly protonated H142 and H143 on the ε site.

QM/DMD Simulations. Different metal variants of HDAC8 might not necessarily have identical equilibrium structures, and therefore, it was important to perform full statistical mechanical equilibration, with the quantum mechanical (QM) treatment of the metals, and the sampling of the protein backbone. Mixed quantum-classical simulations were carried out using QM/DMD,[45] a hybrid quantum mechanics (QM)/discrete molecular dynamics (DMD) method. This method provides the advantages of fast sampling of protein conformations without the need to rely on parametrization of

DOI: 10.1021/acs.jpcb.6b00997
J. Phys. Chem. B 2016, 120, 5884−5895

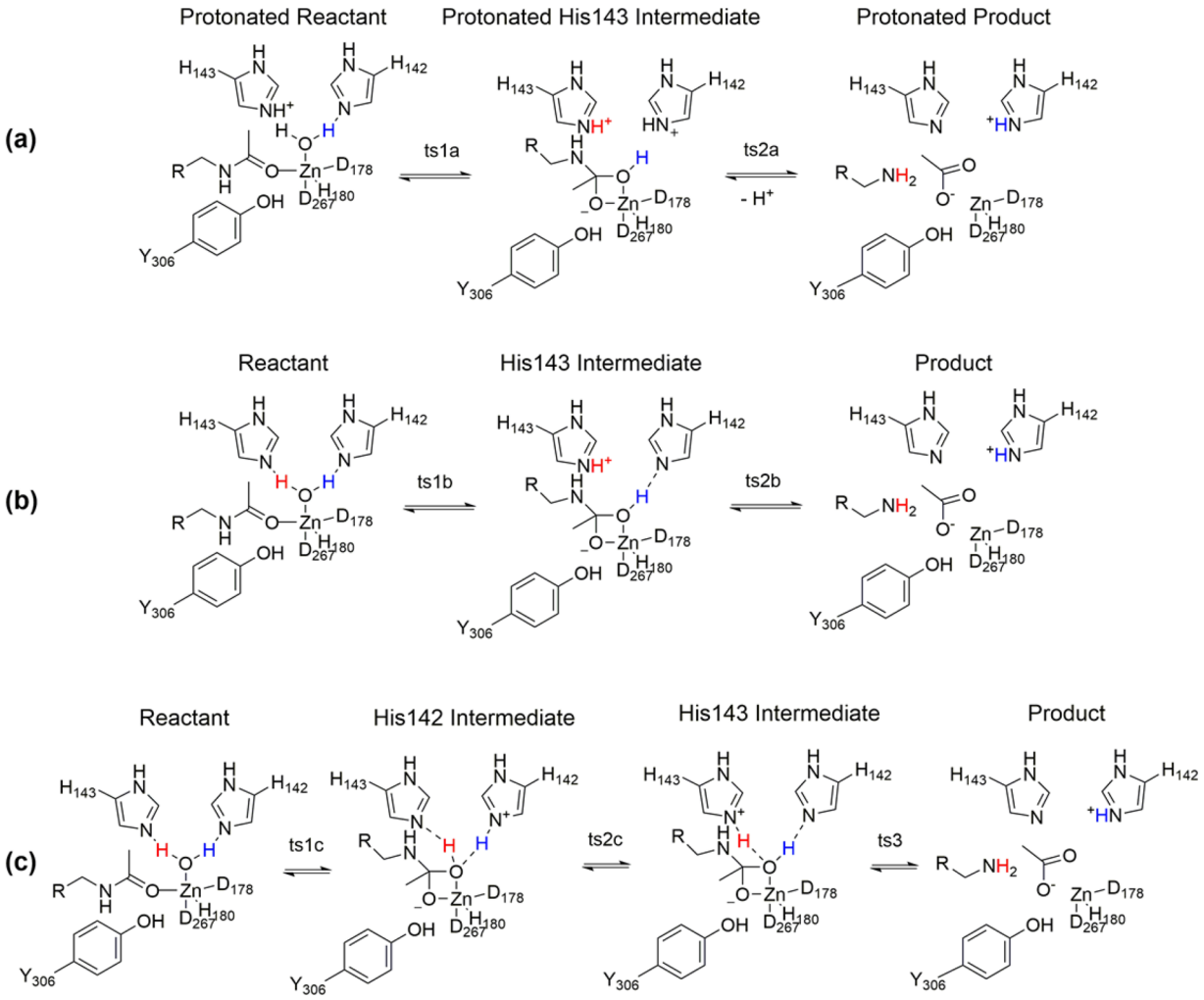

Figure 2. Schematic reaction diagrams for all previously considered HDAC8 mechanisms: Reaction a relies on the unusual initial protonation state of the coordinating His reaction. Further, concerted addition to the carbonyl with transfer of proton to His142, as in reaction a, is found less favorable due to electrostatic effects of the nearby protein (as discussed in the "Contributions outside the QM Subsystem" section later in this paper). Reaction b was originally considered by the Zhang group,[41,42] and reaction c was studied by Chen et al.[60] as an alternative to the Zhang mechanism. Reactions b and c are the mechanisms most studied in this paper. The relevant protons responsible for facilitating these mechanisms are highlighted in red and blue. Mechanism a was not heavily considered due to the requirement that His residues take on an unlikely protonation state at neutral pH.

the classical force field for metal ions. It has been shown to perform very well in the structural and mechanistic studies of natural and modified metalloenzymes.[44,46−50] In QM/DMD, QM calculations are performed using density functional theory (DFT) as implemented in *Turbomole* v6.6.[51] Sampling in the classical regime is carried out using DMD,[43] a variant of a classical MD based on solving energy and momentum conservation equations rather than Newtonian equations of motion. The protein is partitioned into three regions: (1) a QM region, in which atoms can only be moved via a QM optimization (these are the metal and atoms immediately bound to it); (2) a mixed QM−DMD region, in which atoms can be moved by QM or by DMD, depending on the stage of the simulation (this region is discussed separately in the section below; it effectively constitutes a large cluster model of the active site); and (3) a DMD-only region, containing the bulk of the protein. The DMD parameters for the QM−DMD region are adjusted on the fly, based on the QM calculations. Solvent effects are included implicitly in the force field of DMD. In the QM region, solvent has been modeled using COSMO[52] using a dielectric constant ε of 4 (in consideration of the buried active site), and, separately, nonpolarizable point charges (AMBER force field) have been included. All zinc states had their electronic energy and COSMO corrections recomputed using ε of 8 and 20—the resulting energy range was found to be within the expected error of DFT calculations (see Table 4 of the Supporting Information).

Beyond QM/DMD iteration 0, which is a DFT optimization performed on the QM region of the initial structure, each iteration of QM/DMD consists of a DMD step followed by a QM step. To improve sampling, the DMD simulation begins with annealing at the start of each iteration. QM-only atoms are held fixed and a few additional constraints (such as the maximum allowed distance variation between histidine−aspartate dyads) are applied, in accord with previously reported recommendations.[45,46,48,49,53] After the annealing, the temperature is kept low for the final 10 000 DMD time units (0.5 ns), when the data—an ensemble of structures—is collected.

The Kabsch[54] RMSD is computed for all pairwise structures to quantify their geometric similarity. On the basis of the RMSDs, a hierarchical clustering algorithm is used to group the structures into distinct clusters. For this study, the number of

DOI: 10.1021/acs.jpcb.6b00997
J. Phys. Chem. B 2016, 120, 5884−5895

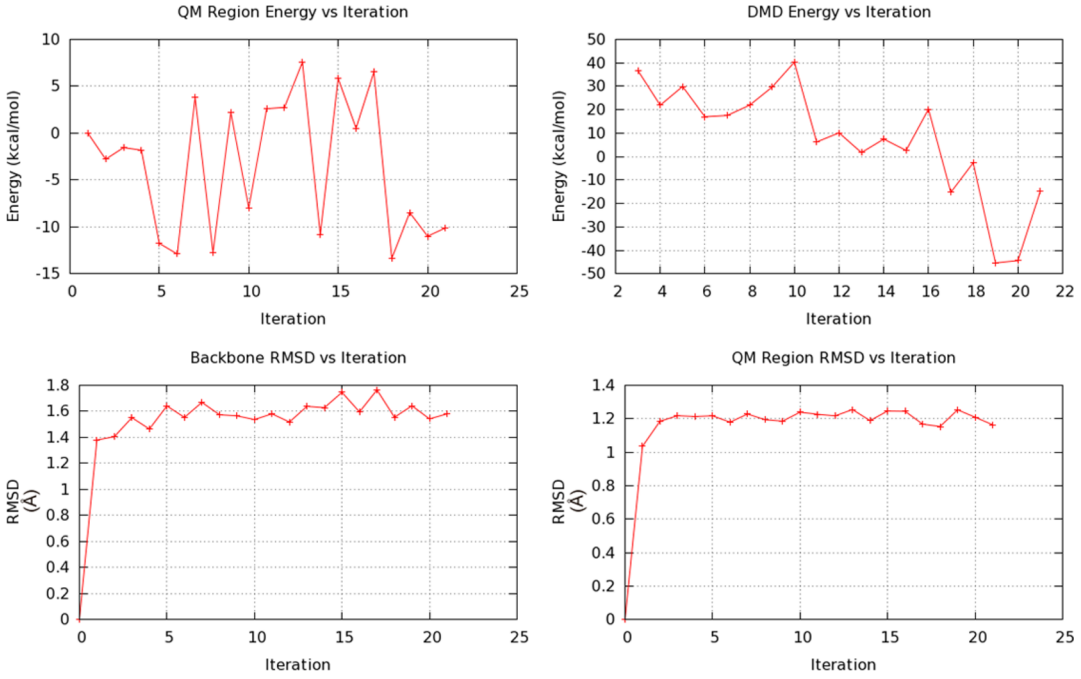

Figure 3. Typical convergence plots of QM/DMD runs. The top left graph displays the energy of the QM active site, and the top right displays the DMD energy of the protein as a function of QM/DMD iteration number. Note that sporadic high-energy structures would be discarded in the iterative procedure. The bottom left displays the convergence of the backbone RMSD, while the bottom right exhibits the convergence of the active site RMSD. A leveled off RMSD graph indicates the lowest energy structures can be weighed on the basis of Boltzmann statistics. This simulation with Zn^{2+} in the active site is representative of all studied systems.

clusters was set as 3. The lowest DMD energy structure within each cluster proceeds to the QM step. The QM step begins by expanding the QM−DMD boundary and cutting the QM−DMD region from the DMD-generated structures. Atoms at the QM−DMD boundary are capped with hydrogen atoms. To maintain the positions dictated by the protein backbone, the boundary atoms and the capping hydrogens are frozen for the duration of the QM step. DFT single point energy calculations are carried out using the TPSS functional.[55,56] The def2-TZVPP basis set[57] is used for the metal atoms, while all other atoms are described by def2-SVP.[57] The Grimme dispersion correction[58] is included for all QM calculations. Structures are assigned a scoring index based on their deviation from the lowest energy QM region and the lowest energy DMD structure found during the iteration. An ideal structure would have both the lowest QM energy and the lowest DMD energy, but the best structure found during each iteration may represent a compromise between the two. As in previous studies, the QM and DMD portions were weighted equally when assigning a scoring value. The QM region of the best-scoring structure is optimized under the same conditions described for the single point energy calculations, followed by removing the capping hydrogens, reinstallation of the QM region into the protein, and shrinking the QM−DMD boundary to the QM-only region. The resulting DMD- and QM-optimized structure is used as a starting structure for the next QM/DMD iteration. The simulations were propagated to convergence in terms of the active site all-atom RMSD, backbone RMSD, QM, and DMD energies, which typically was reached within 20−25 iterations, roughly corresponding to 10 ns of dynamics.

Figure 3 shows typical results of a QM/DMD run, specifically for HDAC8 with Zn^{2+} bound to the divalent site. Across all of the metals in this study, metal coordination largely remains similar as in the Zn^{2+} case. One notable exception is Ni^{2+} which assumes a larger coordination number; Ni^{2+} becomes overcoordinated by acquiring the second oxygen ligand of Asp178.

Large QM Subsystem Requirement. The choice of the QM−DMD subsystem sizes was found to be critical, with the minimal models producing clearly wrong results. The smallest 112-atom QM−DMD subsystem shown in blue in Figure 4 was originally studied. This seemingly reasonable QM−DMD region appeared to be problematic, because upon optimization at the QM level (with any choice for the basis set and DFT method) the substrate acetyl oxygen dissociated from Zn^{2+} (R(O−Zn) = 3.09 Å), whereas in the crystal structure of the Y306F mutant this coordination is present. Over the course of 40 QM/DMD iterations, the substrate remained uncoordinated to the metal, and coordinated instead to Y306. Of course, it is possible that the Y306F mutation itself is responsible for the difference in the substrate binding, and the substrate detachment in the presence of Y306 is therefore mechanistically meaningful (note that the F306Y mutant is catalytically inactive). To rule out this possibility, we also simulated the Y306F mutant in the presence of the substrate. It was found that the substrate still dissociates from the zinc into an unreactive conformation (contrary to the crystal structure), thereby discrediting the choice for the smaller QM−DMD system. Interestingly, in previous studies, this effect was never reported. The implications for the reaction mechanism must be profound, as the detached substrate is not a position conducive to catalysis. We find that a larger QM region is absolutely necessary.

The QM−DMD subsystem was then expanded to include a total of 165 atoms, as seen in Figure 4. Of particular importance is a conserved K^+ ion located within 7 Å of the active site that was investigated in a previous QM/MM study.[41] Single point

DOI: 10.1021/acs.jpcb.6b00997
J. Phys. Chem. B 2016, 120, 5884−5895

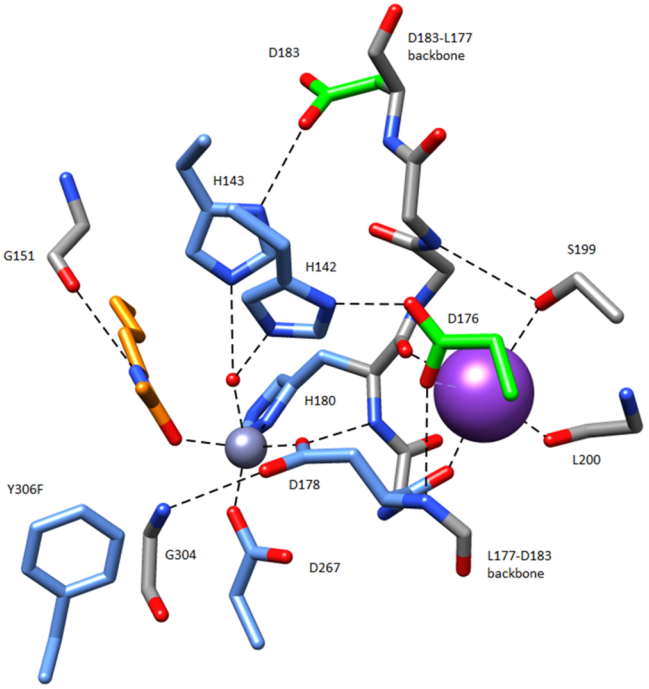

Figure 4. Diagram of residues included in the QM profile in previous and the present studies. The bound substrate is shown in orange. The original work by the Zhang group[41,42,59] included residues colored in blue. The investigation by Chen et al.[60] included the blue residues, as well as the additional residues D176 and D183 in green. The current study expands on both of these by including additional residues colored gray, and the K^+ ion colored purple, as justified in the text.

calculations that included K^+ revealed stabilization of transition states. Furthermore, complexes lacking K^+ were found to have a longer zinc−substrate distance of 2.23 Å, compared to 2.13 Å in the wild-type structure. Thus, K^+ with its minimal coordination sphere was included in our QM system. We argue that, without the coordination sphere, the electric field of K^+ would not be shielded, and thus would be exaggerated. All together, the QM−DMD region consisted of the side chains of H142, H143, D267, and Y306, the backbone chain spanning L177, D178 (with its side chain), L179, H180 (with its side chain), H181, G182, and D183 (with its side chain), the side chain of S199, the backbone of L200, the side chains of the dyad residues D183 and D176 connecting to metal-coordinating H142 and H143, respectively, and the additional G304 and G151. The backbone of the latter two amino acids provided hydrogen bonds to D178, and allowed for its single-dentate coordination to the metal, which in turn left a place for substrate binding. Simulations done with this choice for the QM−DMD region showed a bonding distance of ca. 2.15 Å between Zn^{2+} and the substrate, which is very reasonable. We find this choice for the QM region justified and sufficient.

We note that the choice for the QM−DMD region expands upon prior investigations significantly, and represents the largest studied QM active site. Previous investigations by the Zhang group[41,42,59] (Figure 4, blue) included H142, H143, D178, H180, D267, and Y306, but this provided an incomplete description of the dyad network attached to H142 and H143, whose basicity is the key to the first step of the reaction. The complete QM description of this network was provided by Chen et al.,[60] who included D176 and D183. However, in their work, the influence of the potassium ion was included only via single point calculations. Additional parts not previously considered to be of importance but now included are G182, S199, G303, the carbonyl groups of G304, L200, G151, and the backbones spanning residues L177−D183 (Figure 4, gray).

Mechanistic Study. The QM−DMD region described in the previous section was also used for the subsequent QM-only mechanistic study. All calculations of the stationary points on the reaction profile have been optimized with *Turbomole* v6.6 using the TPSS functional and Def2-TZVPP basis set for all metals, and Def2-SVP basis sets for nonmetal atoms. Spin-unrestricted calculations were performed on all active sites. Re-equilibration of all metals, except Zn and Mg, in low- and high-spin states was attempted. High-spin states were consistently preferred by >10 kcal/mol for all points along the reaction profiles; thus, reaction pathways involving low-spin states were considered uncompetitive and are not included. Vibrational frequency analysis was done using the same level of theory, and the nature of all transition states was determined by the presence of a single imaginary frequency aligned with the reaction coordinate. Single point energy calculations were carried out using the larger Def2-TZVPP basis set for all atoms. We note that the size of the QM region necessary in this work is very large, and more expensive DFT calculations, for example, hybrid functionals, are beyond reach in this context. Nevertheless, we chose to compromise in this way, in view of the identified chemical significance of the large cluster model.

Electron Charge Density Analysis. The quantum theory of atoms in molecules (QTAIM) can be used to understand bonding interactions based on the topology and geometry of the charge density ($\rho(r)$).[61] Topological classifications can be made on the basis of critical points (CPs), i.e., points where the gradient of the charge density vanishes. There are four types of stable CPs in a 3D scalar field such as $\rho(r)$. Maxima generally occur at atomic nuclei and are thus called nuclear CPs. Cage CPs occur inside atomic cages and are local minima in $\rho(r)$. There are also two types of saddle points in $\rho(r)$. The first, a ring CP, has positive curvature in two directions, and is topologically required inside rings of atoms. The other saddle point has one positive curvature and is called a bond CP. This name derives from the fact that the presence of a bond CP is indicative of a ridge of charge density originating at bond CPs and terminating at nuclear CPs. These ridges are called bond paths, since they possess the topological properties imagined for a chemical bond. The magnitude of the charge density at bond CPs often correlates to the strength of interactions between atoms.[61−63] In this work, we used QTAIM to investigate $\rho(r)$ for different metal variants, to elucidate the electronic origin of the calculated mechanistic differences.

The charge density for the reactant geometries of HDAC8 with all six metal ions was calculated with the Amsterdam Density Functional Package (ADF) version 2014.01[64−66] using similar computational parameters as in the QM mechanistic study. A TPSS functional[56,67] and COSMO solvent model with a dielectric constant of 4.0 were utilized. A double ζ quality basis set, DZP, was employed for all atoms except the metal, which was calculated using a triple ζ quality basis set, TZP.[68] Spin-unrestricted calculations were performed on the Zn and Mg active sites, while all other metals were calculated in their high-spin states. The Bondalyzer add-on package in Tecplot[69] was then used to analyze the calculated charge densities.

Born−Oppenheimer Molecular Dynamics (BOMD) Simulations. BOMD simulations were done for the full DFT sampling of the complexes of the studied metals with

DOI: 10.1021/acs.jpcb.6b00997
J. Phys. Chem. B 2016, 120, 5884−5895

organic chelators. This was needed for the assessment of the relative metal binding affinities to the HDAC8 protein, as described below.

RESULTS AND DISCUSSION

1. Catalytic Mechanism. A step toward understanding the chemistry of HDAC8 is elucidating the nature of the catalytic metal ion. Most often it is assumed to be Zn^{2+}. Since the enzyme is functional with Zn^{2+}, this metal becomes a natural suspect, due to its abundance, low toxicity, flexibility of coordination,[70] and fast ligand exchange.[71] However, recent experimental evidence indicates that HDAC with other divalent metals exhibits similar efficacy, sometimes surpassing that of Zn^{2+}. It is particularly noteworthy that Co^{2+} and Fe^{2+} were found to be more active than Zn^{2+}.[37] In this work, we study the Zn^{2+}, Fe^{2+}, Co^{2+}, Ni^{2+}, Mn^{2+}, and Mg^{2+} variants of HDAC8.

In QM/DMD simulations, all metals generally exhibited a distorted square pyramidal geometry. Representative structures were taken from QM/DMD trajectories for the mechanistic study (the corresponding geometries of the active sites are given in the Supporting Information). We examined mechanisms b and c (Figure 2). While part of mechanism c (ts1c) was found to be viable, tsc2 corresponding to the subsequent concerted proton shuttling was not found; thus, further characterization of mechanism c was not pursued.

Mechanism b was found to be a viable catalytic pathway for all studied metals (Figure 5, Table 1). The second transition

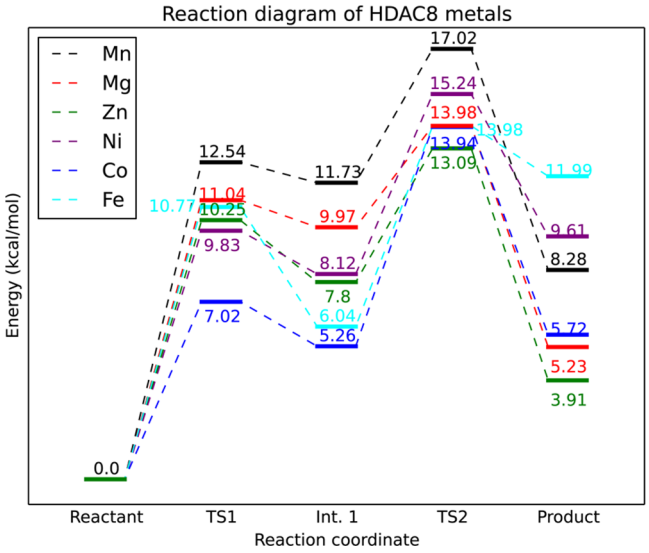

Figure 5. Reaction pathway for HDAC8 and a variety of divalent metal ions (TPSS/Def2-TZVPP+Gibbs free energy corrections//TPSS/Def2-DZVPP, COSMO).

state (ts2b) appears to be rate limiting. This result marks a pronounced deviation from previously published models, which claimed the first transition states, ts1b, to be rate-limiting. This may be an artifact of the QM region being too small in the earlier study. We further find that Zn^{2+} facilitates the fastest catalytic path, followed by Co^{2+}, Mg^{2+}, Fe^{2+}, Ni^{2+}, and Mn^{2+}. This is a notable contrast to experimental assays published by Gantt and co-workers[37] who found Co^{2+} and Fe^{2+} to be the most active, followed by Zn^{2+}, and little reactivity for Ni^{2+} and Mn^{2+}. Because the proton transfer step is rate limiting, it would be reasonable to expect some tunneling of the proton to contribute to the kinetics. A quantum tunneling correction

Table 1. Computed Reaction Profiles with Different Methods and Choices for the Active Sites[a]

	TS1	Int	TS2
full active site, TPSS/Def2-SVP + Gibbs free energy corrections, COSMO	Zn^{2+}: 10.25	Zn^{2+}: 7.80	Zn^{2+}: 13.09
	Fe^{2+}: 10.77	Fe^{2+}: 6.04	Fe^{2+}: 13.98
	Co^{2+}: 7.02	Co^{2+}: 5.26	Co^{2+}: 13.94
	Ni^{2+}: 9.83	Ni^{2+}: 8.12	Ni^{2+}: 15.24
	Mn^{2+}: 12.54	Mn^{2+}: 11.73	Mn^{2+}: 17.02
	Mg^{2+}: 11.04	Mg^{2+}: 9.97	Mg^{2+}: 13.98
full active site, TPSS/Def2-TZVPP + Gibbs free energy corrections,[b] COSMO	Zn^{2+}: 11.42	Zn^{2+}: 10.45	Zn^{2+}: 16.01
	Fe^{2+}: 12.77	Fe^{2+}: 8.50	Fe^{2+}: 16.68
	Co^{2+}: 10.52	Co^{2+}: 7.43	Co^{2+}: 16.82
	Ni^{2+}: 11.50	Ni^{2+}: 10.71	Ni^{2+}: 17.75
	Mn^{2+}: 14.55	Mn^{2+}: 14.54	Mn^{2+}: 20.15
	Mg^{2+}: 13.35	Mg^{2+}: 13.22	Mg^{2+}: 17.47
no K^+ [c]	Zn^{2+}: 11.38	Zn^{2+}: 8.52	Zn^{2+}: 17.00
	Fe^{2+}: 12.23	Fe^{2+}: 8.85	Fe^{2+}: 17.25
	Co^{2+}: 11.53	Co^{2+}: 8.07	Co^{2+}: 18.24
	Ni^{2+}: 11.58	Ni^{2+}: 9.56	Ni^{2+}: 18.26
	Mn^{2+}: 14.19	Mn^{2+}: 12.64	Mn^{2+}: 21.17
	Mg^{2+}: 12.85	Mg^{2+}: 11.01	Mg^{2+}: 18.34
no K^+ nor ligands coordinating it[c]	Zn^{2+}: 9.98	Zn^{2+}: 5.25	Zn^{2+}: 13.74
	Fe^{2+}: 11.74	Fe^{2+}: 5.661	Fe^{2+}: 15.40
	Co^{2+}: 9.60	Co^{2+}: 4.60	Co^{2+}: 13.05
	Ni^{2+}: 11.37	Ni^{2+}: 7.77	Ni^{2+}: 16.12
	Mn^{2+}: 12.86	Mn^{2+}: 8.55	Mn^{2+}: 17.72
	Mg^{2+}: 11.44	Mg^{2+}: 7.45	Mg^{2+}: 14.83
no K^+ site and no D176 and D267[c]	Zn^{2+}: 22.92	Zn^{2+}: 20.95	Zn^{2+}: 22.95
	Fe^{2+}: 23.13	Fe^{2+}: 20.45	Fe^{2+}: 19.75
	Co^{2+}: 23.32	Co^{2+}: 20.95	Co^{2+}: 22.95
	Ni^{2+}: 24.10	Ni^{2+}: 22.24	Ni^{2+}: 23.18
	Mn^{2+}: 25.88	Mn^{2+}: 23.19	Mn^{2+}: 25.40
	Mg^{2+}: 25.11	Mg^{2+}: 23.07	Mg^{2+}: 22.88

[a]For all calculations, the Def2-TZVPP basis set was used for all metals. [b]Gibbs free energy corrections (ZPE + entropic and thermal corrections) were calculated with the Def2-SVP basis set. [c]Single point energies based on the frozen geometries of complete active sites, computed at the TPSS/Def2-SVP level of theory without any free energy corrections.

factor to the rate constant, developed by R. P. Bell,[72] was calculated to be approximately 1.4; thus, it is expected tunneling has some noticeable effect on the kinetics; however, the identity of the metal does not significantly alter this correction.

Why Such a Difference for Different Metals? The main role of the metals in the reaction comes in the first step, in ts1b, where the carbonyl of the substrate is activated for nucleophilic attack. This determines both the activation barrier and the energy of the resultant intermediate, thereby shaping the entire reaction profile. We examine ts1b using QTAIM, to shed light on the electronic effects leading to the metal-dependent performance. The lower energy barriers for Zn^{2+}, Ni^{2+}, Co^{2+}, and Fe^{2+} may be in part due to the higher number of occupied d orbitals than for Mn^{2+} (Mg^{2+} obviously lacking any). The greater number of d electrons implies that orbitals higher up in the enzyme's molecular orbital manifold will be filled. In general, orbitals higher in the manifold are characterized by a greater number of antibonding orbitals and hence more interatomic nodal planes. It is orbitals of this type that stabilize topological rings and cages by contributing density along bond paths though not along nodal planes. This combination leads to

DOI: 10.1021/acs.jpcb.6b00997
J. Phys. Chem. B 2016, 120, 5884−5895

deeper rings and greater curvature at bond CPs. In the plane of a ring of nuclei, as shown in Figure 6, the ring point is a minimum in the charge density. In order for a ring point to exist in this region, a bond path must form between the water molecule and substrate carbonyl.

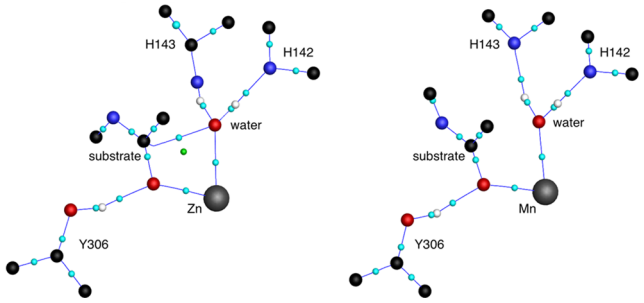

Figure 6. Critical points and bond paths of interest in the active site of HDAC8 with Zn (left) and Mn (right). When Zn is present in the active site, a bond path forms between the water oxygen and the carbon atom from the substrate carbonyl. This topologically necessitates a ring critical point to exist in the active site as well. When Mn is present, no ring CP is found, as there is not a bond path between the water and substrate carbonyl. Ni, Fe, and Co give the same topology as Zn, while Mg has the same topology as Mn. Sphere coloring is as follows: C-black, N-blue, O-red, metal-gray, bond CP-cyan, ring CP-green.

A bond path is present in the reactant state between the substrate carbonyl and water molecule when Zn^{2+}, Ni^{2+}, Fe^{2+}, or Co^{2+} is placed in the active site of HDAC8. This bond path is not present for Mg^{2+} or Mn^{2+}. While this bond is not indicative of a strong interaction (based on low values of charge density at the bond CP as well as the curved nature of the bond path), it still indicates a stabilizing interaction between the water molecule and substrate. It can be seen in mechanism b that, when a proton is transferred from the water molecule to H143, a bond forms between the carbonyl carbon and water oxygen. This bond has already begun to form in the reactant state for Zn^{2+}, Ni^{2+}, Fe^{2+}, and Co^{2+}, which facilitates the removal of a water hydrogen and ultimately lowers the activation energy of this reaction step.

Analysis of Contributions of Protein Parts on the Reaction Profiles. The individual effects of various amino acids in the active site and their role in producing the computed energetics were analyzed. Specifically, we omit certain portions of the active site in the QM site and calculate the energies of the resultant structures without reoptimization. It is recognized that we are making an approximation that the nature of the stationary points would not change significantly upon such changes. This decomposition analysis is highly qualitative, and the goal here is to put all the effects on similar footing with respect to the computational methodology, in order to be able to discuss their respective contribution. Results are summarized in Table 1.

Role of Potassium Ion. Previous studies have suggested that K^+ may play an important electrostatic role in HDAC8 catalysis, but observations have been conflicting.[38,41] It has been generally found that K^+ decreased the rate-limiting transition state barriers, and facilitated a more efficient catalytic path. A reaction pathway using the QM active site in this work without K^+ calculated with a Def2-TZVPP basis set can be found in Table 1.

Within our model, the K^+ ion does influence the catalytic pathway, albeit to a lesser degree than previously thought. It has a mild stabilizing effect on the rate-limiting transition state: for Mn^{2+}, Co^{2+}, and Ni^{2+}, the stabilization is less than 0.5 kcal/mol, while, for Zn^{2+}, there is a destabilization by ∼0.1 kcal/mol. Mg^{2+} remained relatively unaffected by the presence or absence of K^+ in its rate-limiting transition state. It was also found that K^+ had a mild destabilizing influence on ts1b and Int1 with all metals, while having little impact on the product state. Prior investigations have reported more significant stabilizing effects on the rate-limiting step of approximately 4 kcal/mol.[41] Our findings suggest that the impact of potassium as a stabilizing electrostatic component may have been exaggerated in the literature. However, K^+, being so proximal to the active site, might play a critical role in facilitating general active site rearrangement during the reaction.

To additionally assess the role of the K^+ binding site as a whole, a significantly contracted active site was built; it contained the side chains of the residues H142, H143, D178, H180, D267, Y306, D176, and D183 (numbering as in the pdb structure 2V5W), resembling the previously published model by Chen et al.[60] (Figure 4, blue and green residues). In general, the rate-limiting transition state was stabilized by an additional 3−4 kcal/mol. The ts1b was found to be stabilized by approximately 1−2 kcal/mol. Most apparent, the intermediate state was stabilized by ∼5 kcal/mol for all metals, while the product state was destabilized by ∼1 kcal/mol. These findings suggest that K^+ is an important component of the active site, but the effect of this ion needs to be considered in the presence of the shielding ligand environment.

Role of the Catalytic His−Asp Dyad Contacts. The D176 and D267 residues might play a role in positioning and polarizing H142 and H143, both of which were suspected to be catalytic bases in the reaction. The contributions the catalytic dyad contacts lend toward HDAC8 catalysis have been a matter of discussion.[60] An even more contracted QM site was constructed to characterize the effect of the H142−D176 and H143−D267 dyad contacts. This site excluded the D176 and D267 dyad residues. A visual representation of this region can be seen in Figure 4 (blue residues), and resembles some of the first published QM regions.[42] This system in our calculations concurs with current literature, demonstrating the critical importance of these dyad contacts. The His−Asp dyad residues provide exceptional stability to the catalytic pathway. In the absence of these residues, the positioning and protonation sites of H142 and H143 would be adversely affected. Additionally, their removal results in destabilization of the ts2b rate-limiting transition state on the order of ∼5 kcal/mol, and would render HDAC8 extremely slow. However, more generous destabilization is afforded to many other states of the system, which alter the general catalytic landscape. Specifically, the intermediate state increases in energy by 10−12 kcal/mol. Most notably, the ts1b state increases in energy by ∼12 kcal/mol for all metals, rendering this the new rate-limiting transition state for all metals, consistent with the results of prior theoretical investigations considering the same mechanism. Though these effects are exaggerated without geometry optimizations, they still suggest that these dyad contacts are critical to the catalytic function of HDAC8. They most apparently serve to increase the basicity of H142 and H143 and provide stabilization of intermediate states via electrostatics and polarizing hydrogen bonds. These results also demonstrate that these dyad contacts are likely crucial for communicating

DOI: 10.1021/acs.jpcb.6b00997
J. Phys. Chem. B 2016, 120, 5884−5895

with the nearby K^+ binding region. Although the K^+ binding pocket has an overall destabilizing electrostatic effect, it likely allows for configurational rearrangement of the Asp dyad contacts to better coordinate to their respective His partners. This in turn alters the entire landscape of the predicted catalytic path, shifting the rate-limiting transition state from ts1b to ts2b by increasing the basicity of these dyad His residues. The increased basicity, however, means deprotonation of the His residue to the substrate will require higher energy. When these contacts are removed, the energetic landscape reverts back to a shape consistent with, albeit higher in energy, the earliest published theoretical work. Thus, HDAC8 balances electrostatic destabilization with favorable configurational rearrangement to produce the catalytic profile published here.

Contributions outside the QM Subsystem. Early in the mechanistic studies published on HDAC8, the Zhang group showed significant electrostatic contributions of several nearby residues.[42] Most of the residues cited in the Zhang group's early paper have been explicitly included in the 165-atom QM subsystem presented here, sans a His−Glu salt bridge whose effects canceled in the early paper. In order to test for further electrostatic contributions, COSMO solvation of the larger active site was replaced with a system of point charges derived from the AMBER force field,[73−76] as implemented in Nwchem.[77] The resulting point charges were transferred back to *Turbomole* for recalculation of all intermediates and transition states for mechanism b. Current implementations prohibit the combination of implicit solvation and electrostatic embedding, and thus, we are forced to consider these effects separately. This, however, does not alter our ultimate conclusions, which will be presented below. The mechanism was found to not change, but there are some important energetic differences summarized by the example in Figure 7.

As Figure 7 shows, the electrostatic environment, treated as explicit nonpolarizable point charges, favors mechanism b, which starts with the proton shuttled directly to H143, while it disfavors mechanism c where the proton first moves to the H142. Thus, the electrostatic contributions from outside the already-large QM subsystem do not significantly alter the mechanism of action; however, they still help direct the relative pathway.

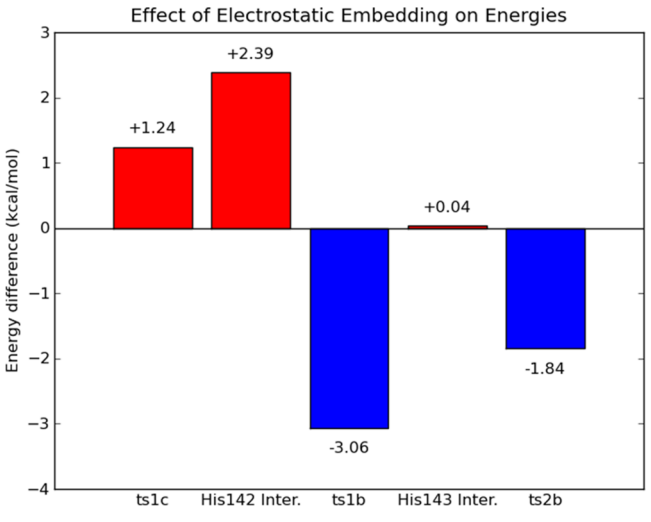

Figure 7. Difference in Gibbs free energies for the most active Co^{2+}−HDAC8, relative to the reactant state, upon electrostatic embedding. An increase in energy indicates embedding has a destabilizing effect, while a decrease in energy indicates a stabilizing effect of embedding. States ts1c and His142 intermediate are only considered in mechanism c, while ts1b, His143 intermediate, and ts2b are considered in the current mechanism.

2. Metal Binding. We have also explored how metal binding affinity may affect the overall reactivity of HDAC8's deacetylating action. Gantt and co-workers have shown that several of the metal ions in this investigation were inactive *in vitro*;[37] however, many of the computed rate-limiting transition state energies found in this paper are well under the ceiling of catalytic inactivity. It is possible that the binding affinity of each metal toward HDAC8 could have an effect on *in vitro* catalytic activity, and may play an important role in *in vivo* metal selection. Here, we attempt to elucidate how significant this effect might be.

To this end, first, we have compared the accuracy of DFT to the experiment, in assessing metal binding, using the experimentally known stability constants of the complexes of the studied metals with GEDTA and DTPA (Table S1).[78] From these stability constants, the free energies of reactions (1−4) in Figure 8 are known (Table S1). Further, from $\Delta\Delta G$ of reactions 1 and 2, one can close the thermodynamic cycle for DPTA on the upper left in Figure 8. Analogously, one can close the cycle for GEDTA on the upper right in Figure 8, using $\Delta\Delta G$ of reactions 3 and 4. Through combination of these two cycles, one can then calculate the ΔG of metal swapping between the two chelators

$$\text{DTPA-M}_a^{2-} + \text{GEDTA-M}_b^{2-} \rightarrow \text{DTPA-M}_b^{2-} + \text{GEDTA-M}_a^{2-}$$

bypassing the complicated calculation of the solvated metal ions, $M_a^{2+}(aq)$ and $M_b^{2+}(aq)$. The ΔG values of metal swapping were calculated both from the experimental data and with DFT. The structures of the metal−GEDTA and metal−DTPA complexes that we used were geometry-optimized and also subjected to 5 ps of BOMD, to verify the ground state geometries (they are shown in Figure S1). To avoid the additional desolvation complications, polydentate ligation of the chelating agent was selected such that the bound metal had no solvent access, preventing explicit water coordination, and allowing for the exclusive use of COSMO. The theoretical and experimental ΔG of metal swapping can be found in Table S2. The computed ΔG values were found to be in good agreement with experiment, having an average of 0.5 ± 1.5 kcal/mol error (Table S3). Despite small absolute errors, there is a notable bias across substitutions involving Mn^{2+}—the authors concede this source of error may be due to some deficiency in the representation of the metal ion *in silico* or in describing its coordination mode.

This methodology was then applied to a theoretical metal swap between DTPA and HDAC8

$$\text{DTPA-M}_b^{2-} + \text{HDAC8-Co}^{2-} \rightarrow \text{DTPA-Co}^{2-} + \text{HDAC8-M}_b^{2-}$$

using ΔG of reactions 1 and 2 and 5 and 6 in Figure 8, and with M_a set to Co^{2+} as a reference. The above reaction can be paired with the experimental ΔG of reactions shown in Table S1, to yield ΔG of the following process:

DOI: 10.1021/acs.jpcb.6b00997
J. Phys. Chem. B 2016, 120, 5884−5895

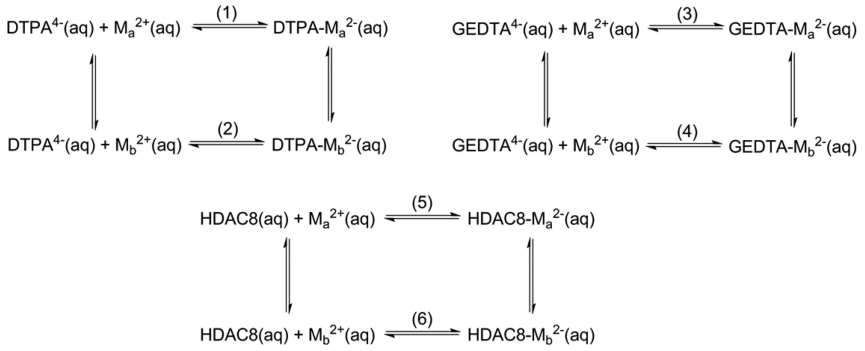

Figure 8. Schematic of all considered thermodynamic cycles exploited for relative binding affinities.

$$M_b^{2+}(aq) + \text{HDAC8-}Co^{2-} \rightarrow Co^{2+}(aq) + \text{HDAC8-}M_b^{2-}$$

This gives the desired relative affinities of the different metals to HDAC8, collected in Table 2.

Table 2. ΔΔG of Binding between Metal Ions and HDAC8, Relative to Co^{2+}

metal	ΔΔG binding, kcal/mol
Co^{2+}	0.00
Fe^{2+}	3.52
Mg^{2+}	16.75
Mn^{2+}	6.28
Ni^{2+}	−4.33
Zn^{2+}	1.99

As one may see, Co^{2+} is predicted to bind to HDAC8 very strongly. It is followed by Zn^{2+} and Fe^{2+}. Mn^{2+} and Mg^{2+} have considerably smaller affinities for HDAC8. However, Ni^{2+} is calculated to have the highest binding affinity toward HDAC8 among all the studied metals. This ordering can be related to the active site geometries and corresponding electronic effects. A particularly direct interaction exists between the metal and H180, which is therefore highly important for metal binding. For this residue, the relationship between binding affinity and the amount of charge density at the Nε−metal bond CP is linear (Figure 9). The charge density at the bond CP is a consequence of σ-bonding and π-back-donation with the available d-AOs on the given metal. Mg, lacking any occupied d-AOs, has a significantly lower charge density at the bond CP and lower binding affinity than any of the transition metals, despite having a relatively short bond length (which is simply due to its smaller size). Thus, the geometric and electronic parameters of this Nε−metal bond can serve as predictors of the metal binding affinity in this case.

Metal Binding Affinity and Reactivity. In protein assay experiments, the purified protein is often equilibrated in a high concentration solution of the desired metal ions. These ions are then purged from the mixture, leaving the protein−metal complex behind. Under these conditions, the metal ions exist in equilibrium between protein and solution. If metal binding affinity is too small, this could render the system less active than demonstrated by computational studies. This difference in binding affinity could also play a key role in the overall catalytic activity of enzyme capable of utilizing different metals, and elucidate its preference for any one particular ion. We now aim to evaluate the ability for the protein to retain a metal and

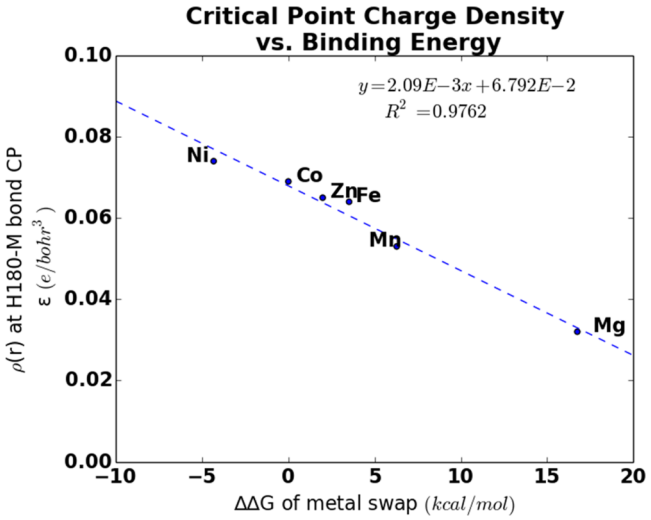

Figure 9. Trends between QTAIM $\rho(r)$ at bond CP and ΔΔG of metal swapping.

subsequently use it for catalysis. Our simple probabilistic model captures the combined effects of metal-binding equilibration and subsequent catalysis relative to any particular ion. In the equation

$$K_{rel} = k_{cat} \cdot K_{binding}$$

K_{rel} stands for the relative total catalytic activity of a particular protein−metal complex, k_{cat} represents the catalytic activity as determined by QM mechanistic analysis, and $K_{binding}$ embodies the relative equilibrium binding constant between a metal and an enzyme. These values can be represented as Boltzmann distributions utilizing the above computed quantities in catalysis and binding affinity to yield

$$K_{rel} = \exp\left(-\frac{\Delta G^{\ddagger}}{RT}\right)\exp\left(-\frac{\Delta\Delta G_{binding}}{RT}\right)$$

whose values are summarized in Table 3. An alternative two-state ensemble model for binding was also used to assess catalytic efficacy (Figure S2), which agreed qualitatively with the current simple model for a reasonable range of binding affinities.

This model qualitatively predicts the trend seen in catalytic activity for these metals in experiment, though the trend is slightly perturbed,[37] either due to experimental errors or inaccuracies of our model. Co^{2+} is predicted as the most active, followed by Zn^{2+} and Fe^{2+}. Additionally, noncatalytic metal

DOI: 10.1021/acs.jpcb.6b00997
J. Phys. Chem. B 2016, 120, 5884−5895

Table 3. Predicted Relative Total Catalytic Activities[a]

	K_{rel}	normalized	k_{cat} (s^{-1}), from experiment[37]
Ni^{2+}	1.89×10^{-8}	1.00	N/A
Co^{2+}	7.64×10^{-11}	4.03×10^{-3}	1.2
Zn^{2+}	1.27×10^{-11}	6.70×10^{-4}	0.90
Fe^{2+}	1.75×10^{-13}	9.24×10^{-6}	0.48
Mn^{2+}	1.37×10^{-17}	7.11×10^{-10}	N/A
Mg^{2+}	1.46×10^{-23}	7.71×10^{-16}	N/A

[a]Binding affinity energies were taken relative to Co^{2+}. Normalized values appear on the right column, relative to the predicted most active metal ion−protein complex.

Mn^{2+} is predicted as being 5 orders of magnitude less reactive than Fe^{2+}. This is due to both manganese's poor binding affinity to the active site of HDAC8 and its higher ΔG_{rxn}. Zn^{2+} is predicted to be less catalytically active than Co^{2+}, despite its low reaction barrier, due to its poor affinity, while Co^{2+} exhibits high catalytic activity in spite of a higher reaction barrier. Fe^{2+} competes with Co^{2+} and Zn^{2+}, even though it has a higher reaction barrier than Zn^{2+}. However, Ni^{2+}, experimentally shown to be inactive, is a clear outlier, and is predicted to be exceptionally catalytic, due to high binding affinity. This may be an artifact of the simple model, since coordination of Ni^{2+} is different from those of other metals. Mg^{2+} examined in this work was not tested experimentally. We show that, even though it has reasonable reaction energetics, its affinity to HDAC8 is very low, and Mg^{2+} is ultimately predicted by our calculations to have a very low catalytic activity. Thus, it is obvious that the d-AO structure is required in HDAC8, despite the simple Lewis acid catalysis performed by the metal in this enzyme.

CONCLUSIONS

We computationally studied the metal-dependent mechanism and performance of the Fe^{2+}, Co^{2+}, Mn^{2+}, Ni^{2+}, Mg^{2+}, and Zn^{2+} variants of the HDAC8 enzyme, in corroboration with and also beyond the existing experimental data. It was found that an unusually large QM region was required in both mixed quantum-classical dynamics simulations and subsequent mechanistic study (the QM region is nearly doubled as compared to all previous published studies), to properly describe this enzyme. This expansion has significant impacts on the overall catalytic ability of HDAC8, and predicts the rate-determining step of the reaction to be different from previous findings. Instead of the nucleophilic attack, the second proton transfer step appears to be rate-determining. We have shown that the His−Asp dyads coordinating to the metal bound water are critical in facilitating catalysis, and defining the new rate-determining step. We also have shown that the nearby K^+ ion together with its coordination sphere has only a mild stabilizing electrostatic effect, in contrast to previously published results. We additionally devise a scheme for estimating the relative binding affinities of different metals to the protein. In combination with the reaction free energies, this quantity allows us to reproduce the experimentally observed trend in metal-dependent performance of HDAC8, with the exception of Ni^{2+}. Co^{2+} is predicted to be the most active catalytic metal in HDAC8, followed by Zn^{2+} and Fe^{2+}, whereas Mn^{2+} and Mg^{2+} are several orders of magnitude less active. We note that our model does not include any information about relative metal availability, and other reactivity in the cellular environment, which might further impact the apparent preference for different metal variants.

ASSOCIATED CONTENT

Supporting Information

The Supporting Information is available free of charge on the ACS Publications website at DOI: 10.1021/acs.jpcb.6b00997.

XYZ coordinates of all reactant states, literature binding energies and calculated "metal swap" energies, single point energies at different values of the dielectric value in COSMO, and a catalytic model utilizing a two-state ensemble for $K_{binding}$ over a range of possible binding affinities for Co (PDF)

AUTHOR INFORMATION

Corresponding Author

*E-mail: ana@chem.ucla.edu. Phone: +1 (310) 825-3769.

Notes

The authors declare no competing financial interest.

ACKNOWLEDGMENTS

This work was supported by the NSF CAREER Award CHE1351968 to A.N.A. and ONR Grant No. N00014-10-1-0838 to M.E.E. and A.M. Computational resources were provided by the UCLA-IDRE cluster. This paper is dedicated to the birthday of Prof. William Gelbart, who is an invaluable colleague, mentor, and a wonderful friend.

REFERENCES

(1) Yang, X. J.; Seto, E. HATs and HDACs: From Structure, Function and Regulation to Novel Strategies for Therapy and Prevention. *Oncogene* **2007**, *26*, 5310−5318.

(2) Wang, Z.; Zang, C.; Rosenfeld, J. A.; Schones, D. E.; Barski, A.; Cuddapah, S.; Cui, K.; Roh, T. Y.; Peng, W.; Zhang, M. Q.; et al. Combinatorial Patterns of Histone Acetylations and Methylations in the Human Genome. *Nat. Genet.* **2008**, *40*, 897−903.

(3) Kouzarides, T. Acetylation: A Regulatory Modification to Rival Phosphorylation? *EMBO J.* **2000**, *19*, 1176−1179.

(4) Choudhary, C.; Kumar, C.; Gnad, F.; Nielsen, M. L.; Rehman, M.; Walther, T. C.; Olsen, J. V.; Mann, M. Lysine Acetylation Targets Protein Complexes and Co-Regulates Major Cellular Functions. *Science* **2009**, *325*, 834−840.

(5) Kouzarides, T. Chromatin Modifications and Their Function. *Cell* **2007**, *128*, 693−705.

(6) Iwabata, H.; Yoshida, M.; Komatsu, Y. Proteomic Analysis of Organ-Specific Post-Translational Lysine-Acetylation and -Methylation in Mice by Use of Anti-Acetyllysine and -Methyllysine Mouse Monoclonal Antibodies. *Proteomics* **2005**, *5*, 4653−4664.

(7) Kim, S. C.; Sprung, R.; Chen, Y.; Xu, Y.; Ball, H.; Pei, J.; Cheng, T.; Kho, Y.; Xiao, H.; Xiao, L.; et al. Substrate and Functional Diversity of Lysine Acetylation Revealed by a Proteomics Survey. *Mol. Cell* **2006**, *23*, 607−618.

(8) Xie, H.; Bandhakavi, S.; Roe, M. R.; Griffin, T. J. Preparative Peptide Isoelectric Focusing as a Tool for Improving the Identification of Lysine-Acetylated Peptides from Complex Mixtures. *J. Proteome Res.* **2007**, *6*, 2019−2026.

(9) Gu, W.; Roeder, R. G. Activation of P53 Sequence-Specific DNA Binding by Acetylation of the P53 C-Terminal Domain. *Cell* **1997**, *90*, 595−606.

(10) Imhof, A.; Yang, X. J.; Ogryzko, V. V.; Nakatani, Y.; Wolffe, A. P.; Ge, H. Acetylation of General Transcription Factors by Histone Acetyltransferases. *Curr. Biol.* **1997**, *7*, 689−92.

(11) Yang, X. J.; Gregoire, S. Metabolism, Cytoskeleton and Cellular Signalling in the Grip of Protein Nepsilon - and O-Acetylation. *EMBO Rep.* **2007**, *8*, 556−562.

(12) Starai, V. J.; Celic, I.; Cole, R. N.; Boeke, J. D.; Escalante-Semerena, J. C. Sir2-Dependent Activation of Acetyl-CoA Synthetase by Deacetylation of Active Lysine. *Science* **2002**, *298*, 2390−2392.

DOI: 10.1021/acs.jpcb.6b00997
J. Phys. Chem. B 2016, 120, 5884−5895

(13) Hallows, W. C.; Lee, S.; Denu, J. M. Sirtuins Deacetylate and Activate Mammalian Acetyl-CoA Synthetases. *Proc. Natl. Acad. Sci. U. S. A.* **2006**, *103*, 10230−10235.
(14) Schwer, B.; Bunkenborg, J.; Verdin, R. O.; Andersen, J. S.; Verdin, E. Reversible Lysine Acetylation Controls the Activity of the Mitochondrial Enzyme Acetyl-CoA Synthetase 2. *Proc. Natl. Acad. Sci. U. S. A.* **2006**, *103*, 10224−10229.
(15) L'Hernault, S. W.; Rosenbaum, J. L. Chlamydomonas A-Tubulin Is Posttranslationally Modified by Acetylation on the E-Amino Group of a Lysine. *Biochemistry* **1985**, *24*, 473−478.
(16) Piperno, G.; Fuller, M. T. Monoclonal Antibodies Specific for an Acetylated Form of A-Tubulin Recognize the Antigen in Cilia and Flagella from a Variety of Organisms. *J. Cell Biol.* **1985**, *101*, 2085−2094.
(17) Kamine, J.; Elangovan, B.; Subramanian, T.; Coleman, D.; Chinnadurai, G. Identification of a Cellular Protein That Specifically Interacts with the Essential Cysteine Region of the HIV-1 Tat Transactivator. *Virology* **1996**, *216*, 357−366.
(18) Reifsnyder, C.; Lowell, J.; Clarke, A.; Pillus, L. Yeast Sas Silencing Genes and Human Genes Associated with Aml and HIV-1 Tat Interactions Are Homologous with Acetyltransferases. *Nat. Genet.* **1996**, *14*, 42−49.
(19) Allfrey, V. G.; Faulkner, R.; Mirsky, A. E. Acetylation and Methylation of Histones and Their Possible Role in the Regulation of RNA Synthesis. *Proc. Natl. Acad. Sci. U. S. A.* **1964**, *51*, 786−794.
(20) Phillips, D. M. The Presence of Acetyl Groups of Histones. *Biochem. J.* **1963**, *87*, 258−63.
(21) Gallinari, P.; Di Marco, S.; Jones, P.; Pallaoro, M.; Steinkuhler, C. HDACs, Histone Deacetylation and Gene Transcription: From Molecular Biology to Cancer Therapeutics. *Cell Res.* **2007**, *17*, 195−211.
(22) Finnin, M. S.; Donigian, J. R.; Cohen, A.; Richon, V. M.; Rifkind, R. A.; Marks, P. A.; Breslow, R.; Pavletich, N. P. Structures of a Histone Deacetylase Homologue Bound to the Tsa and Saha Inhibitors. *Nature* **1999**, *401*, 188−193.
(23) Hodawadekar, S. C.; Marmorstein, R. Chemistry of Acetyl Transfer by Histone Modifying Enzymes: Structure, Mechanism and Implications for Effector Design. *Oncogene* **2007**, *26*, 5528−5540.
(24) Haberland, M.; Montgomery, R. L.; Olson, E. N. The Many Roles of Histone Deacetylases in Development and Physiology: Implications for Disease and Therapy. *Nat. Rev. Genet.* **2009**, *10*, 32−42.
(25) Smith, B. C.; Denu, J. M. Chemical Mechanisms of Histone Lysine and Arginine Modifications. *Biochim. Biophys. Acta, Gene Regul. Mech.* **2009**, *1789*, 45−57.
(26) Yang, X. J.; Seto, E. The Rpd3/Hda1 Family of Lysine Deacetylases: From Bacteria and Yeast to Mice and Men. *Nat. Rev. Mol. Cell Biol.* **2008**, *9*, 206−218.
(27) Bolden, J. E.; Peart, M. J.; Johnstone, R. W. Anticancer Activities of Histone Deacetylase Inhibitors. *Nat. Rev. Drug Discovery* **2006**, *5*, 769−84.
(28) Paris, M.; Porcelloni, M.; Binaschi, M.; Fattori, D. Histone Deacetylase Inhibitors: From Bench to Clinic. *J. Med. Chem.* **2008**, *51*, 1505−1529.
(29) Marks, P. A.; Breslow, R. Dimethyl Sulfoxide to Vorinostat: Development of This Histone Deacetylase Inhibitor as an Anticancer Drug. *Nat. Biotechnol.* **2007**, *25*, 84−90.
(30) Bradner, J. E.; West, N.; Grachan, M. L.; Greenberg, E. F.; Haggarty, S. J.; Warnow, T.; Mazitschek, R. Chemical Phylogenetics of Histone Deacetylases. *Nat. Chem. Biol.* **2010**, *6*, 238−243.
(31) Suzuki, N.; Suzuki, T.; Ota, Y.; Nakano, T.; Kurihara, M.; Okuda, H.; Yamori, T.; Tsumoto, H.; Nakagawa, H.; Miyata, N. Design, Synthesis, and Biological Activity of Boronic Acid-Based Histone Deacetylase Inhibitors. *J. Med. Chem.* **2009**, *52*, 2909−2922.
(32) Gregoretti, I. V.; Lee, Y. M.; Goodson, H. V. Molecular Evolution of the Histone Deacetylase Family: Functional Implications of Phylogenetic Analysis. *J. Mol. Biol.* **2004**, *338*, 17−31.
(33) Somoza, J. R.; Skene, R. J.; Katz, B. A.; Mol, C.; Ho, J. D.; Jennings, A. J.; Luong, C.; Arvai, A.; Buggy, J. J.; Chi, E.; et al. Structural Snapshots of Human HDAC8 Provide Insights into the Class I Histone Deacetylases. *Structure* **2004**, *12*, 1325−1334.
(34) Vannini, A.; Volpari, C.; Filocamo, G.; Casavola, E. C.; Brunetti, M.; Renzoni, D.; Chakravarty, P.; Paolini, C.; De Francesco, R.; Gallinari, P.; et al. Crystal Structure of a Eukaryotic Zinc-Dependent Histone Deacetylase, Human HDAC8, Complexed with a Hydroxamic Acid Inhibitor. *Proc. Natl. Acad. Sci. U. S. A.* **2004**, *101*, 15064−15069.
(35) Vannini, A.; Volpari, C.; Gallinari, P.; Jones, P.; Mattu, M.; Carfi, A.; De Francesco, R.; Steinkuhler, C.; Di Marco, S. Substrate Binding to Histone Deacetylases as Shown by the Crystal Structure of the HDAC8-Substrate Complex. *EMBO Rep.* **2007**, *8*, 879−884.
(36) Dowling, D. P.; Gantt, S. L.; Gattis, S. G.; Fierke, C. A.; Christianson, D. W. Structural Studies of Human Histone Deacetylase 8 and Its Site-Specific Variants Complexed with Substrate and Inhibitors. *Biochemistry* **2008**, *47*, 13554−13563.
(37) Gantt, S. L.; Gattis, S. G.; Fierke, C. A. Catalytic Activity and Inhibition of Human Histone Deacetylase 8 Is Dependent on the Identity of the Active Site Metal Ion. *Biochemistry* **2006**, *45*, 6170−6178.
(38) Gantt, S. L.; Joseph, C. G.; Fierke, C. A. Activation and Inhibition of Histone Deacetylase 8 by Monovalent Cations. *J. Biol. Chem.* **2010**, *285*, 6036−6043.
(39) de Ruijter, A. J.; van Gennip, A. H.; Caron, H. N.; Kemp, S.; van Kuilenburg, A. B. Histone Deacetylases (HDACs): Characterization of the Classical HDAC Family. *Biochem. J.* **2003**, *370*, 737−49.
(40) Anzellotti, A. I.; Farrell, N. P. Zinc Metalloproteins as Medicinal Targets. *Chem. Soc. Rev.* **2008**, *37*, 1629−1651.
(41) Wu, R.; Wang, S.; Zhou, N.; Cao, Z.; Zhang, Y. A Proton-Shuttle Reaction Mechanism for Histone Deacetylase 8 and the Catalytic Role of Metal Ions. *J. Am. Chem. Soc.* **2010**, *132*, 9471−9479.
(42) Corminboeuf, C.; Hu, P.; Tuckerman, M. E.; Zhang, Y. Unexpected Deacetylation Mechanism Suggested by a Density Functional Theory QM/MM Study of Histone-Deacetylase-Like Protein. *J. Am. Chem. Soc.* **2006**, *128*, 4530−4531.
(43) Shirvanyants, D.; Ding, F.; Tsao, D.; Ramachandran, S.; Dokholyan, N. V. Discrete Molecular Dynamics: An Efficient and Versatile Simulation Method for Fine Protein Characterization. *J. Phys. Chem. B* **2012**, *116*, 8375−8382.
(44) Valdez, C. E.; Gallup, N. M.; Alexandrova, A. N. Co^{2+} Acireductone Dioxygenase: Fe^{2+} Mechanism, Ni^{2+} Mechanism, or Something Else? *Chem. Phys. Lett.* **2014**, *604*, 77−82.
(45) Sparta, M.; Shirvanyants, D.; Ding, F.; Dokholyan; Nikolay, V.; Alexandrova; Anastassia, N. Hybrid Dynamics Simulation Engine for Metalloproteins. *Biophys. J.* **2012**, *103*, 767−776.
(46) Sparta, M.; Alexandrova, A. N. How Metal Substitution Affects the Enzymatic Activity of Catechol-O-Methyltransferase. *PLoS One* **2012**, *7*, e47172.
(47) Nechay, M. R.; Valdez, C. E.; Alexandrova, A. N. Computational Treatment of Metalloproteins. *J. Phys. Chem. B* **2015**, *119*, 5945−5956.
(48) Valdez, C. E.; Sparta, M.; Alexandrova, A. N. The Role of the Flexible L43-S54 Protein Loop in the CcrA Metallo-β-Lactamase in Binding Structurally Dissimilar β-Lactam Antibiotics. *J. Chem. Theory Comput.* **2013**, *9*, 730−737.
(49) Nedd, S.; Redler, R. L.; Proctor, E. A.; Dokholyan, N. V.; Alexandrova, A. N. Cu,Zn-Superoxide Dismutase without Zn Is Folded but Catalytically Inactive. *J. Mol. Biol.* **2014**, *426*, 4112−4124.
(50) Sparta, M.; Valdez, C. E.; Alexandrova, A. N. Metal-Dependent Activity of Fe and Ni Acireductone Dioxygenases: How Two Electrons Reroute the Catalytic Pathway. *J. Mol. Biol.* **2013**, *425*, 3007−3018.
(51) Ahlrichs, R.; Bär, M.; Häser, M.; Horn, H.; Kölmel, C. Electronic Structure Calculations on Workstation Computers: The Program System Turbomole. *Chem. Phys. Lett.* **1989**, *162*, 165−169.
(52) Klamt, A.; Schuurmann, G. Cosmo: A New Approach to Dielectric Screening in Solvents with Explicit Expressions for the Screening Energy and Its Gradient. *J. Chem. Soc., Perkin Trans. 2* **1993**, 799−805.
(53) Valdez, C. E.; Alexandrova, A. N. Why Urease Is a Di-Nickel Enzyme Whereas the CcrA β-Lactamase Is a Di-Zinc Enzyme. *J. Phys. Chem. B* **2012**, *116*, 10649−10656.

DOI: 10.1021/acs.jpcb.6b00997
J. Phys. Chem. B 2016, 120, 5884−5895

(54) Kabsch, W. A Solution for the Best Rotation to Relate Two Sets of Vectors. *Acta Crystallogr., Sect. A: Cryst. Phys., Diffr., Theor. Gen. Crystallogr.* **1976**, *32*, 922−923.
(55) Perdew, J. P.; Wang, Y. Accurate and Simple Analytic Representation of the Electron-Gas Correlation Energy. *Phys. Rev. B: Condens. Matter Mater. Phys.* **1992**, *45*, 13244−13249.
(56) Tao, J.; Perdew, J. P.; Staroverov, V. N.; Scuseria, G. E. Climbing the Density Functional Ladder: Nonempirical Meta-Generalized Gradient Approximation Designed for Molecules and Solids. *Phys. Rev. Lett.* **2003**, *91*, 146401.
(57) Weigend, F.; Ahlrichs, R. Balanced Basis Sets of Split Valence, Triple Zeta Valence and Quadruple Zeta Valence Quality for H to Rn: Design and Assessment of Accuracy. *Phys. Chem. Chem. Phys.* **2005**, *7*, 3297−3305.
(58) Grimme, S. Accurate Description of Van Der Waals Complexes by Density Functional Theory Including Empirical Corrections. *J. Comput. Chem.* **2004**, *25*, 1463−1473.
(59) Wu, R.; Hu, P.; Wang, S.; Cao, Z.; Zhang, Y. Flexibility of Catalytic Zinc Coordination in Thermolysin and HDAC8: A Born−Oppenheimer Ab Initio QM/MM Molecular Dynamics Study. *J. Chem. Theory Comput.* **2010**, *6*, 337−343.
(60) Chen, K.; Zhang, X.; Wu, Y.-D.; Wiest, O. Inhibition and Mechanism of HDAC8 Revisited. *J. Am. Chem. Soc.* **2014**, *136*, 11636−11643.
(61) Bader, R. F. W. *Atoms in Molecules: A Quantum Theory*; Oxford University Press: Oxford, U.K., 1990.
(62) Matta, C. F.; Boyd, R. J. *The Quantum Theory of Atoms in Molecules*; Wiley-VCH Verlag GmbH & Co. KGaA: Weinheim, Germany, 2007.
(63) Boyd, R. J.; Choi, S. C. Hydrogen Bonding between Nitriles and Hydrogen Halides and the Topological Properties of Molecular Charge Distributions. *Chem. Phys. Lett.* **1986**, *129*, 62−65.
(64) te Velde, G.; Bickelhaupt, F. M.; Baerends, E. J.; Fonseca Guerra, C.; van Gisbergen, S. J. A.; Snijders, J. G.; Ziegler, T. Chemistry with Adf. *J. Comput. Chem.* **2001**, *22*, 931−967.
(65) Fonseca Guerra, C.; Snijders, G. J.; te Velde, G.; Baerends, J. E. Towards an Order-N Dft Method. *Theor. Chem. Acc.* **1998**, *99*, 391−403.
(66) Baerends, E. J.; Ziegler, T.; Atkins, A. J.; Autschbach, J.; Bashford, D.; Bérces, A.; Bickelhaupt, F. M.; Bo, C.; Boerrigte, P. M.; Cavallo, L.; Chong, D. P.; et al. *Adf2014*; Vrije Universiteit: Amsterdam, The Netherlands, 2014.
(67) Staroverov, V. N.; Scuseria, G. E.; Tao, J.; Perdew, J. P. Comparative Assessment of a New Nonempirical Density Functional: Molecules and Hydrogen-Bonded Complexes. *J. Chem. Phys.* **2003**, *119*, 12129−12137.
(68) Van Lenthe, E.; Baerends, E. J. Optimized Slater-Type Basis Sets for the Elements 1−118. *J. Comput. Chem.* **2003**, *24*, 1142−56.
(69) *Tecplot 360, R1*; Tecplot, Inc.: Seattle, WA, 2015.
(70) McCall, K. A.; Huang, C.; Fierke, C. A. Function and Mechanism of Zinc Metalloenzymes. *J. Nutr.* **2000**, *130*, 1437s−1446s.
(71) Sousa, S. F.; Fernandes, P. A.; Ramos, M. J. The Carboxylate Shift in Zinc Enzymes: A Computational Study. *J. Am. Chem. Soc.* **2007**, *129*, 1378−1385.
(72) Bell, R. P. *The Tunnel Effect in Chemistry*; University Press: Cambridge, U.K., 1980.
(73) Cornell, W. D.; Cieplak, P.; Bayly, C. I.; Gould, I. R.; Merz, K. M.; Ferguson, D. M.; Spellmeyer, D. C.; Fox, T.; Caldwell, J. W.; Kollman, P. A. A Second Generation Force Field for the Simulation of Proteins, Nucleic Acids, and Organic Molecules. *J. Am. Chem. Soc.* **1995**, *117*, 5179−5197.
(74) Wang, J.; Cieplak, P.; Kollman, P. A. How Well Does a Restrained Electrostatic Potential (RESP) Model Perform in Calculating Conformational Energies of Organic and Biological Molecules? *J. Comput. Chem.* **2000**, *21*, 1049−1074.
(75) Hornak, V.; Abel, R.; Okur, A.; Strockbine, B.; Roitberg, A.; Simmerling, C. Comparison of Multiple Amber Force Fields and Development of Improved Protein Backbone Parameters. *Proteins: Struct., Funct., Genet.* **2006**, *65*, 712−725.
(76) Wang, J.; Wolf, R. M.; Caldwell, J. W.; Kollman, P. A.; Case, D. A. Development and Testing of a General Amber Force Field. *J. Comput. Chem.* **2004**, *25*, 1157−1174.
(77) Valiev, M.; Bylaska, E. J.; Govind, N.; Kowalski, K.; Straatsma, T. P.; Van Dam, H. J. J.; Wang, D.; Nieplocha, J.; Apra, E.; Windus, T. L.; et al. Nwchem: A Comprehensive and Scalable Open-Source Solution for Large Scale Molecular Simulations. *Comput. Phys. Commun.* **2010**, *181*, 1477−1489.
(78) Dojindo.com Metal Chelates - Analytical & Biological Products. pp 252−253 (accessed Jan 31, 2016).

DOI: 10.1021/acs.jpcb.6b00997
J. Phys. Chem. B 2016, 120, 5884−5895